Int J Adv Manuf Technol (2018) 94:3117–3129
DOI 10.1007/s00170-017-0897-6

ORIGINAL ARTICLE

Parameter optimization of friction stir welding of cryorolled AA2219 alloy using artificial neural network modeling with genetic algorithm

K. Kamal Babu [1] · K. Panneerselvam [1] · P. Sathiya [1] · A. Noorul Haq [1] · S. Sundarrajan [2] · P. Mastanaiah [3] · C. V. Srinivasa Murthy [3]

Received: 28 April 2017 / Accepted: 27 July 2017 / Published online: 10 August 2017

Abstract In this paper, parameter optimization of FSW of cryorolled AA2219 alloy was carried out to obtain defect free weld joint with maximum weld strength. To achieve this, artificial neural network (ANN) was used to model the relationship between the input parameters and the mechanical and corrosion properties (output) of the weld joints. The optimal FSW parameters were determined by genetic algorithm (GA). The feasible solution of the GA was tool rotational speed of 1005 rpm, tool travel speed of 20 mm/min and tool tilt angle of 3°. The feasible parameter was used to weld and check the ability of the parameter to produce better weld joint than the L_9 orthogonal array parameters. The weld, subjected to the confirmation test, was investigated by means of metallurgical, mechanical, and corrosion testing. This process reduces the costs associated with trial runs to obtain optimal parameters and also the production cost of the cryorolled (CR) plate which is high.

Keywords Cryorolled AA2219 · FSW · ANN · GA · Microstructure analysis · Corrosion test

✉ P. Sathiya
psathiya@nitt.edu

[1] Department of Production Engineering, National Institute of Technology, Tiruchirappalli, Tamilnadu 620015, India

[2] National Institute of Technology, Tiruchirappalli, Tamilnadu 620015, India

[3] Defence Research and Development Laboratory, Hyderabad, Telengana 500058, India

1 Introduction

Friction stir welding (FSW) process is one of the novel techniques invented by Thomas et al. in the year 1991 at The Welding Institute in UK. This joining technique was mainly used for the aluminum alloys. Nowadays, FSW plays a vital role in the field of solid state metal joining processes for non-ferrous alloys and is gradually replacing the conventional arc weld joining process with aluminum alloys. FSW also eliminates the radiation effect and harmful emission of gases during the fusion welding process.

During the FSW process, a rotating tool with shoulder surface and unique pin design is plunged in between the abutting surfaces of the plates to be joined. Due to the contact of the shoulder with the top surface of the joining portion, heat is generated and the metal flows from retreating section to advancing section by means of tool rotational speed, tool inclination and tool travel made along the joining line [1]. Thus, the frictional heat makes the material soft and allows the material to flow along the welding line without reaching the melting point. Finally, the weld joint is fabricated by the thrust force of the tool shoulder [2]. The heat treated aluminum AA2219 alloy has superior strength to weight ratio and the alloy is one of the best materials to satisfy the required properties for aerospace structural applications and cryogenic fuel tanks [3].

The tensile property of the FSW joints depends on the tool rotational speed, tool travel speed, and tilt angle. Better tensile strength was achieved by optimizing the process parameters of FSW [4]. The FSW parameters which are spindle speed, tool travel speed, and downward force data were considered to maximize the tensile strength. The FSW parameters were modeled with response surface methodology (RSM) and the results were optimized with fuzzy grey relational analysis [5]. The positioning of weld plates during welding played a vital

role in determining the strength of the joint. The Taguchi's L_9 orthogonal array was used for optimizing the rotational speed, dwell time, tool plunge depth, and tilt angle. Also, the analysis of variance (ANOVA) demonstrated that the tool rotational speed was the most dominant parameter that influenced the strength of the joint. Conformation testing on the results was performed to prove the optimal parameters resulted in the maximum tensile strength of the weld joint [6, 7]. Tool pin profile and shoulder to pin diameter ratio is one of the influencing factors on the tensile strength of the FSW joint, which was analyzed with Taguchi L_{16} orthogonal array [8].

The RSM and multi-objective Taguchi method were used to optimize the FSW process parameter against the response of the weld quality, tensile strength, and hardness value [9, 10]. The findings of most influential factors from the Taguchi in the FSW process showed that the tool rotational speed contributed 41%, transverse speed contributed 33%, and axial force 21% on the ultimate tensile strength (UTS) of the FSW joint [11, 12]. Shojaeefard et al. studied multi-objective optimization to find out the better combination of the process parameters. Here, artificial neural network (ANN) was used to model the relationship between the decision variables and the quality of the weld and the PSO was used to optimize the Pareto solutions. The Order Preference by Similarity to the Ideal Solution (TOPSIS) was used to find out the best compromise solution [13]. Gupta et al. found the significant process parameters using the hybrid approach of grey relational analysis (GRA) with principal component analysis (PCA). The optimum welding parameters with significant contribution were welding speed (42.8%), tool rotational speed (30.7%), and shoulder (25.93%) [14].

Shojaeefard et al. investigated the influence of transverse and rotational speeds on HAZ breadth, peak temperature, and welding force. A hybrid multi-objective optimization was used with ANN modeling to investigate the effects of parameter on weld during FSW and TOPSIS was used to acquire the optimal solution at the Pareto frontier [15]. Dewan et al. in their work compared ANN model and a newly developed Adaptive Neuro-Fuzzy Inference System (ANFIS) model in optimizing FSW parameters. The authors concluded that the ANFIS model produced better result than the ANN [16, 17]. The maximization of mechanical properties of FSW joint was optimized by using simulated annealing algorithm with ANFIS [18]. The ANN model was used on the L_9 Taguchi design of laser welding of NiTinol. Here, four learning algorithms were used namely Legvenberg-Marquardt back propagation, batch back propagation, quick propagation, and incremental back propagation. On comparing the four algorithms, it was found that the Legvenberg-Marquardt model gave the least error. Genetic algorithm (GA) was used to find the optimal process parameter [19].

A set of L_{25} Taguchi orthogonal array of Flux cored arc welding process parameters was optimized using ANN simulation by MATLAB using particle swarm optimization (PSO) algorithm [20]. Khethier et al. worked with a design of experiments and Taguchi technique for friction stir spot welding parameter optimization on dissimilar Al alloys (AA2024 and AA5754) and found that the tool pin profile had a higher influence than the tool rotational speed and plunging time [21]. ANN was used to find out the best FSW tool among different tool pin profiles and it was found that the weld joint made by conical pin tool with thread exhibits maximum tensile strength and microhardness [22]. Similarly, ANN-GA was used to find out the optimal FSW parameters like tool travel speed, rotation speed and offset distance to obtain better UTS on dissimilar joints of AA5052 and AISI 304. From the ANN-GA optimization, it was determined that for the inputs of 500 rpm, 80 mm/min and 2-mm tool offset produced maximum tensile strength [24]. Panneerselvam et al. used hybrid ANN-GA optimization to obtain maximum joint strength by using frictional vibration joining method for plastics sheets and the optimal parameters were tested with conformation test [25].

FSW process parameters optimization for Al1080 alloy was carried out with GONNS (Genetically Optimized Neural Network Systems) intelligent decision-making system to train the network and the results were fed into one or more ANN and optimized by GA to maximize the mechanical properties [26]. Anand et al. attempted to reduce the weld heat affected portion of friction welded joint using ANN modeling and maximize the mechanical properties [27]. Likewise, GA was used to maximize the joint strength of friction stir welded ferritic stainless steel AISI 430. It was found that for 1120 rpm rotational speed, 125 mm/min welding speed, 4.5 kN axial force with 0° tool tilt angle better tensile strength was obtained compared to the base material [28]. ANN modeling and comparative study of GA and PSO were worked out in drilling operation and found that the GA provides better solution than the PSO [29].

The process parameter optimization for FSW on AA2219 was done by experimental design and it was found that increasing tool rotational speed increased the welding strength [30–32] and also the lowering welding speed gave more UTS [33]. The low axial force caused less UTS value [34], and the high axial thrust force increased the hardness of the material [35, 36]. In FSW on copper plate, the increasing welding speed reduced the peak temperature of the weld zone and it caused finer grain refinement at the nugget portion [37]. But in the friction stir spot welding of 2024 aluminum alloy, the tool plunge rate and dwell time influenced the heat generation and weld joint efficiency [38]. The result of the RSM parameter optimization of FSW on pure copper alloy, showed the tool rotational speed was the major influencing parameter on the UTS of the weld joint [39], and also the ANOVA gave more than 95% of confidence level of result [40, 41]. The geometrical shape of the FSW tool pin influenced the microstructural

changes on the weldment and strength [42, 43]. Also, the tool pin profile facilitated the proper material flow around the tool during FSW process [44].

The FSW on Al 7075 and its process parameter optimization were carried out using ANFIS and it was found that the square pin tool profile with welding speed of 100 mm/min, tool rotational speed of 1400 rpm with 7.5 kN axial load produced the highest joint efficiency of the weld [45]. FSW on Cu-Zn alloy was carried out, its parameters and output responses were correlated by using RSM and it was reported that the Zn content dissolution increased with a decrease of tool rotational speed and welding speed [46]. A second order regression model was used to analyze the process parameter and UTS of the plasma-MIG hybrid weld AA2219 joints and it was reported that the maximum of UTS achieved was 289.6 MPa [47]. The analysis of variance was commonly employed to predict the accuracy level of optimization model [48]. Nowadays, the current manufacturing scenario focuses on the product lifecycle management (from beginning to end of the product), particularly managing the different process of the product manufacturing cycle that generates large amount of data. Here, it becomes necessary to optimize the parameters of a particular process, flow of process and process constraints [49]. From the literature, it can be found that the predicting accuracy of ANN model is more efficient than the RSM. Also the RSM needs more number of experimental data than the ANN modeling and also it delivers very less error on the predicted results with minimum number of experimental runs.

From the literature survey, it is found that a lot of research was done for the optimization of process parameters of fusion and solid state welding processes with different optimization techniques. But there were no prior optimization works for FSW on CR AA2219 material. Hence, this present study concentrates on the FSW parameter optimization of the cryorolled AA2219-T87 material.

The cryorolling process is one of the foremost severe plastic deformation methods to produce ultrafine grain structure to obtain improved strength of the alloy. The main scope of using ANN-GA optimization technique in this present FSW on CR AA2219 material study was to obtain the optimal process parameters to get better quality weld joints with high strength. As the cost of cryorolled processed material is quite expensive, this work can reduce the number of trial run experiments. Therefore, it becomes necessary to optimize the input FSW process parameters. Figure 1 shows the flow chart of ANN and GA methodology followed for this present work.

Here, three ANN models namely Batch Back Propagation (BBP), Quick Propagation (QP), and Incremental Back Propagation (IBP) were used. The input parameters were optimized by using GA. Here, the ANN was employed to model the mathematical associations between control parameters and tensile strength, microhardness and corrosion current density, while the GA was used to evaluate the optimal of the inputs.

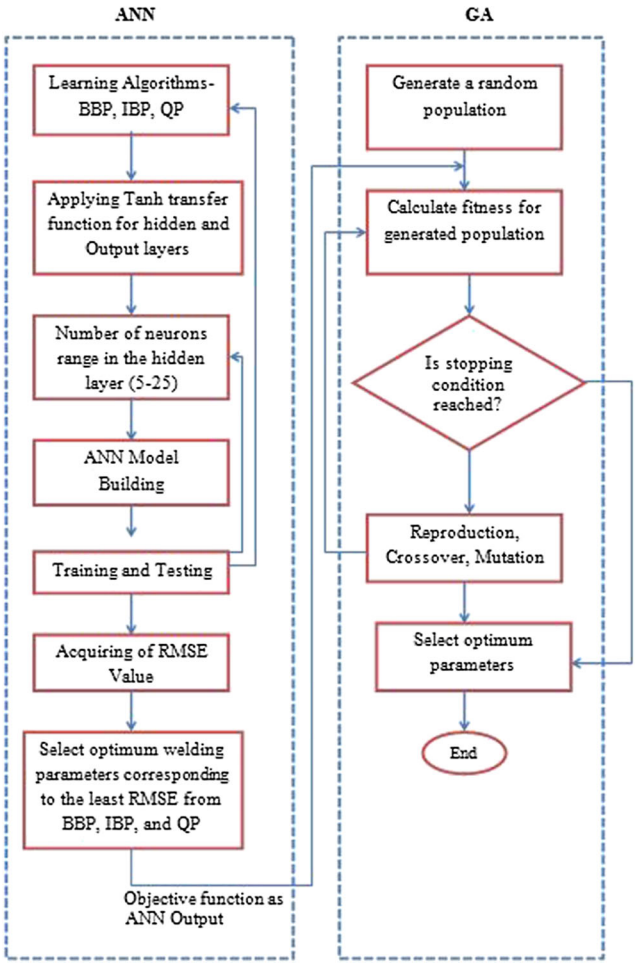

Fig. 1 Logical flow chart of integrated ANN–GA model

Consequently, the overall target of this work is to establish the set of process parameters that provide weldment with the optimal quality characteristics.

2 Materials and methods

The AA2219 material is basically Al-Cu-Mn based alloy which is usually difficult to join. Here, the properties of the base alloy were improved by severe plastic deformation mechanism with the cryorolling process. The AA2219 plate was cut into 200 × 100 × 22.5 mm thick and the surface was cleaned before starting of cryorolling process. During cryorolling, the AA2219 plates were kept in liquid nitrogen for 30 min and the plates were subsequently rolled with the heavy duty rolling mills. There was 46% percentage of reduction in thickness in base AA2219 material with no change in chemical composition. Table 1 presents the chemical composition of the AA2219 material.

The final size of the cryorolled plate was 12.2 mm thick and CR plate was cut into 150 × 100 × 6 mm thick plates by electro discharge wire cutting process to weld. The FSW of

Table 1 Chemical composition of AA2219-T87 alloy

Element	Cu	Mn	Zr	V	Ti	Fe	Si	Al
Weight percent	6.26	0.4	0.15	0.11	0.07	0.2	0.12	Balance

CR AA2219 material was conducted on four axis BISS friction stir welding machine with Taguchi L_9 experimental design. The FSW machine is shown in Fig. 2.

Table 2 presents enhanced properties of ultimate tensile strength, microhardness, and corrosion resistance of cryorolled AA2219 alloy. Here, it is be found that the properties of the CR AA2219 material got improved with respect to the base alloy. This was due to the effect of the cryorolling process.

Figure 3 presents the FSW hexagonal pin tool profile and the same was used to join the CR material during the L_9 experiment. The non-consumable tool was machined from M42 grade super high-speed steel bar. Figure 4 presents the tensile test specimen of the FSW joint. The tensile samples were prepared according to the ASME E-8M standards. The tensile test was conducted with the tensometer (make: FIE-Bluestar, India; Model: UNITEK−94100).

The Vickers microhardness test was performed based on the ASTM E384 standard with a load set at 0.5 kg and dwell time equal to 10 s (make: Wilson Hardness VICKERS 402MVD). The welded joint portion was cut and polished with different grade emery sheets. Further polishing was performed with disc polishing machine with alumina slurry and finally mirror finished with diamond cloth. The macro and microscopic analysis were performed with the optical macro and microscopy (Olympus BX51M). The HITACHI-S3000-N scanning electron microscopy was used to perform energy-dispersive X-ray spectroscopy (EDX) test on the weldment. The potentiodynamic polarization test was carried out with the computerized electrochemical system. The test utilized a saturated calomel reference electrode (SCE), graphite counter electrode (reference electrode), and the working electrode as

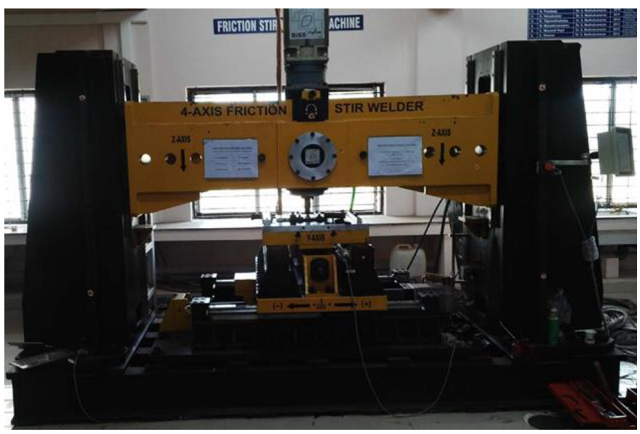

Fig. 2 Friction stir welding machine

Table 2 Mechanical and corrosion properties of cryorolled AA2219 alloy

Material	Ultimate strength (MPa) ±2	Microhardness ($HV_{0.5}$) ±1	Corrosion resistance I_{corr} value ($\mu A/cm^2$) ±2
Cryorolled AA2219	463.93	168	85.14

corrosion specimen. The open circuit potential was obtained for the specimen by the initial holdup of 3600 s. The corrosion current density was found out for all weldment specimens with scan rate of 0.5 mV/s from −1 V/SCE to +1 V/SCE. The image analyzer was used to measure the corrosion pit details. Table 3 presents the process parameters of the FSW experiments and their range.

Table 4 presents the results of the output responses of the Taguchi L_9 experimental run. Here, the input parameters were tool rotational speed, travel speed, and axis inclination of the FSW tool. Also the results of Table 4 express the ultimate tensile strength values of the nine weld experiments. Here, the three tensile specimens were cut from each experimental weld runs and the average of three UTS test results of each experiment weld joint were noted in Table 4. Likewise,

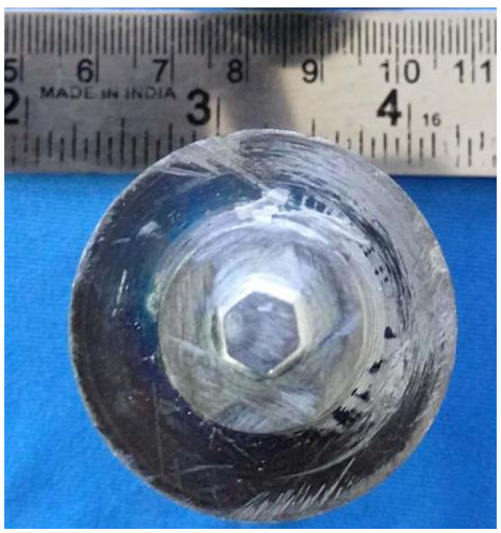

Fig. 3 Hexagonal pin FSW tool

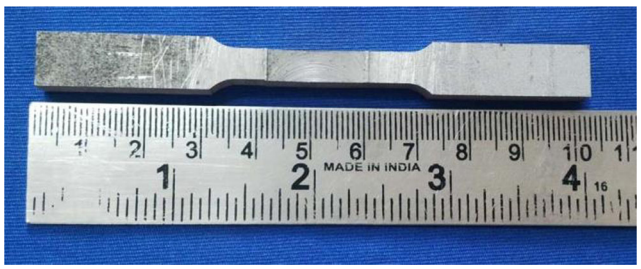

Fig. 4 Tensile sample of the friction stir welded joint

Table 3 Process parameters of FSW and their levels

Symbol	Parameters	Units	Levels		
			1	2	3
X	Tool rotational speed	rpm	1000	1250	1500
Y	Tool travel speed	mm/min	20	25	30
Z	Tool tilt angle	Degree	2.5	3	3.5

the microhardness of the weld nugget portion was measured at three different locations along the middle of the nugget in lateral direction to the weld joint. Since the corrosion test (potentiodynamic polarization test) process time was too long and very expensive, only one corrosion test was conducted on the weld nugget portion for each weld experimental run.

3 Results and discussion

3.1 Artificial neural network

The ANN was developed based on the functional aspects of the biological neurons and it is one of the mathematical models used for mapping a non-linear relationship between a set of inputs and their corresponding responses. In ANN, every neuron is connected with each other through links called as synapses. Also, every synapse has a weight value associated with it that causes an excitatory or inhibitory response. The modeling and optimization analysis were carried out using Neural Power professional version 2.5 software. There are two steps involved in the neural network modeling, which is training and testing. In this software, the experimental data was split into 80 and 20%. Neural power software consists of up to five learning algorithms. The following algorithms BBP, IBP, and QP with one hidden layer were selected to train the ANN model. The hidden layer neurons were selected in the range of 5 to 25. The number of iterations was fixed for each type of model at 10000.

Here, from Table 4, the 2nd experiment results to 8th experimental results were (80% of experimental data) utilized in the training phase of the algorithm and that training results were presented in Table 5. Then, the remaining 20% of experimental results in Table 4 (experimental result 1st and 9th) were used to test the capability of the ANN to forecast the output responses by feeding only the input responses. The 80 to 20% ratio of training data to forecasting data respectively can be selected in all possible ways from the whole experimental results. This is one of the significant features of the Neural Power professional version 2.5 software. The software also facilitates modeling of the data with several learning algorithms (The training with the different models are presented in Table 5). For the present study, seven FSW trial experimental results with their inputs (experiment 2nd to 8th) were selected to train the ANN model designed in Neural Power professional. The experiments 1 and 9 were selected as test data to determine the forecasting accuracy of the ANN and the same was presented in Table 7. From the result of the ANN modeling with the three algorithms, the least root mean square error (RMSE) value was selected as best which was calculated from Eq. 1

$$RMSE = \sqrt{\frac{1}{n}\sum_{i=1}^{n}(P-E)^2} \quad (1)$$

where

E actual value
P forecasted value
n number of experiments in the data set

It was observed from many of the literatures, the tanh function yielded better result than the other function [19]. So, the Hyperbolic tanh function was utilized as activation

Table 4 Taguchi L_9 orthogonal array and experimental results (input and output response)

Exp.No	Tool rotational speed (rpm)	Tool travel speed (mm/min)	Tool tilt angle (deg.)	Ultimate tensile strength (MPa) ±2	Microhardness ($HV_{0.5}$) ±1	Corrosion resistance I_{corr} value ($\mu A/cm^2$) ±2
1	1000	20	2.5	290	115	28.5
2	1000	25	3	331	126	14.4
3	1000	30	3.5	285	118	31.5
4	1250	20	3	302	124	18.9
5	1250	25	3.5	177	96	362.4
6	1250	30	2.5	127	90	424.3
7	1500	20	3.5	213	98	153
8	1500	25	2.5	184	99	232.2
9	1500	30	3	128	83	426.1

Table 5 Average RMSE values for different learning algorithms

No of hidden layer neurons	Average RMSE		
	BBP	IBP	QP
5	0.0099997	0.019916	0.4836
7	0.0089991	0.036574	0.5667
9	0.0099892	0.0099802	0.43143
14	0.0099809	0.0099913	0.24356
16	0.018637	0.089475	0.099818
18	0.511771	0.017012	0.09929
23	0.11101	0.99999	0.0982
25	0.06269	0.99989	0.059938

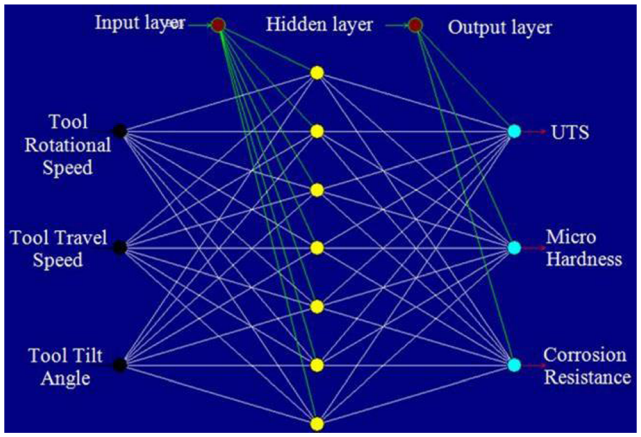

Fig. 5 ANN structure

in both hidden and output layers. Hyperbolic tanh equation is presented in Eq. 2

$$F(x) = \frac{1-exp(-ax)}{1+exp(-ax)} \tag{2}$$

Table 5 presents the mean RMSE value of the different learning algorithms by changing the number of hidden layer nodes.

From Table 5, the least RMSE value was found with BBP algorithm having seven hidden layer nodes. The difference between the experimental output values and training results was obtained from the ANN of BBP learning algorithm (with experimental input and output) for seven neurons and is presented in Table 6. The ANN has a single input layer having three input nodes, single hidden layer having seven neurons and a single output layer having three output responses. The structure of the ANN is as shown in Fig. 5.

The difference between the 8th and 9th experiment results and the training data obtained from BBP (with experimental input and without output) learning algorithm with seven neurons are presented in Table 7.

The experimental results and calculated ANN results of UTS, microhardness, and corrosion current density were presented in Tables 6 and 7. The tool rotational speed parameter's contribution in influencing the weldment quality was 36%, the tool travel speed contributed 35%, and the tool tilt angle contributed 29% on the weld joint performance. Also, it is found that the experimental and calculated results were very close. The experimental result lines were almost coinciding with the predicted values by BBP with seven neurons. The GA optimization was carried out to determine the optimal welding parameters by employing the BBP model.

3.2 Genetic algorithm

Genetic algorithm is a metaheuristic optimization method to solve both unconstrained and constrained problems and is influenced by evolution. The algorithm continually regenerates the population of individual solutions to find a more optimal solution set with respect to the previous iteration. During each iteration, the GA selects solution sets from the population using a randomizing method as parents to generate offspring for the next iteration. The algorithm can be made to reach the optimum by generating offspring from parents that are the most optimal in the current solution set. GA relies on reaching the optimum beginning from a randomly generated solution

Table 6 Difference between the experimental output and training data output (with experimental input and output) of BBP learning algorithm with seven neurons in the hidden layer

Exp. No	Ultimate tensile strength (MPa)			Microhardness ($HV_{0.5}$)			Corrosion resistance I_{corr} value ($\mu A/cm^2$)		
	Exp. results	ANN results	Difference	Exp. results	ANN results	Difference	Exp. results	ANN results	Difference
2	331	330.98	0.023741	126	126.01	0.0054019	14.4	14.406	0.0056256
3	285	285	0.0045919	118	118	0.0009991	31.5	31.499	0.0006336
4	302	302.01	0.0071165	124	124	0.0029101	18.9	18.891	0.0093354
5	177	177	0.0021978	96	96.001	0.0007011	362.4	362.4	0.0027912
6	127	127.01	0.013657	90	89.996	0.0037053	424.3	424.28	0.016838
7	213	213	0.0002565	98	98	0.000129	153	153	0.0004291
8	184	184	0.0042901	99	99.001	0.0011322	232.2	232.2	0.0034639

Table 7 Difference between the experimental output and training data output (with experimental input and without output) of BBP learning algorithm with seven neurons in the hidden layer

Exp. No	Ultimate tensile strength (MPa)			Microhardness $HV_{0.5}$			Corrosion resistance I_{corr} value ($\mu A/cm^2$)		
	Exp. results	ANN results	Diff.	Exp. results	ANN results	Diff.	Exp. results	ANN results	Diff.
1	184	184.00006	0.00006	99	98.999969	0.000031	232.2	232.20027	0.00027
9	128	127.69541	0.3046	83	88.905982	5.9060	426.1	420.73954	5.36046

set. By changing the number of population or adjusting the bounds of the parameters, an optimal solution can be reached by running several times. The fundamental steps involved in genetic algorithm are listed below.

1. Initializing the population randomly
2. Objective function evaluation
3. Fitness function finding.
4. Iteratively perform genetic operations random selection, crossover, and mutation until the algorithm converges to optimal point.

The GA optimization process was performed by means of Neural Power Professional 2.5 version software. The objective function derived from BBP learning algorithm was passed onto the GA algorithm module. The selection of parameter for genetic algorithm was by trial and error method. Eventually, the parameters of the GA like population size, crossover rate and mutation rate were selected from the following literature [19].

Size of randomly generated population: 100.

Rate of crossover: 0.9.

Rate of mutation: 0.01.

Criteria for selection: random selection.

Type of crossover: single point.

The range of bound values for tool rotational speed: 1000 and 1500 rpm.

The range of bound values for welding speed: 20 and 30 mm/min.

The range of bound values for tool tilt angle: 2.5° to 3.5°.

3.3 Confirmation test

The confirmation experimentation was done with feasible solution and their results are tabulated in Table 8.

Table 8 shows the calculated ANN optimal solution of input parameters and its relevant calculated output responses. The feasible solution was taken from the nearest round off value of optimal solution for the convenience to carry out the confirmation test. After confirmation FSW experimentation with the feasible solution, the FSW joint was subjected to tensile, microhardness and potentiodynamic polarization test and the results were tabulated in the Table 8. From the results, it is found that the optimal results of the UTS, microstructure and corrosion current densities were closer with the conformation FSW joint results. Also the percentage of error was calculated between the calculated ANN and confirmation experimental results. The percentage of error was minimal and also within the range of acceptance.

3.4 Metallurgical studies

Figure 6a, b presents microstructure of base AA2219 material and cryorolled AA2219 material respectively. The microstructure of the base AA2219 material (Fig. 6a) consists of dark intermetallic compounds with larger grain boundaries. The main precipitate compound of AA2219 alloy is Al_2Cu and a few of Al_6Mn and Al_7Cu_2Fe compounds spread over in the Al matrix. Owing to the cold working and aging treatment, the precipitates were formed in both stable and metastable state in the cast alloy. The presence of the dark intermetallic particles in Fig. 6a, b were θ phase coarser or stable (Al_2Cu) precipitates and the metastable precipitates were not visible in the optical microscope. The average grain size of the base alloy was 68 μm and the same was measured with the line intercept method.

Figure 6b presents the microstructure image of the cryorolled AA2219 material. Here, the grains were elongated in the rolling direction of the material. Due to the rolling

Table 8 Confirmation test results

Experiment	Tool rotational speed (rpm)	Tool travel speed (mm/min)	Tool tilt angle (deg.)	Ultimate tensile strength (MPa)	Microhardness $HV_{0.5}$	Corrosion resistance I_{corr} value ($\mu A/cm^2$)
Optimal solution	1005.659	20.034	2.954	341.27	127.91	12.627
Feasible solution	1005	20	3	–	–	–
Confirmation test results	1005	20	3	333.5	131	13.5
Percentage error				2.27	2.35	6.46

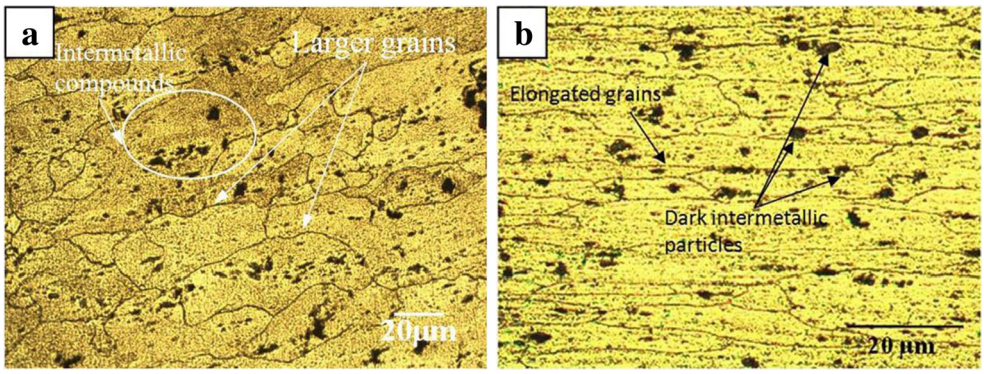

Fig. 6 **a**, **b** Microstructure of Base AA2219 and CR AA2219 material, respectively

carried out under severe strain, the larger grains of the AA2219 alloy were fragmented and compressed in nature. During the cryorolling, cross-slip occurred in the grains and it caused the fragmentation of grains and precipitates in the alloy. The CR AA2219 material had average grain size of 36 μm. The bimodal grain distribution of coarser elongated grain islands with sever dislocation tangles can give high strength without major loss in ductility.

The confirmation experiment was done with the feasible solution, with tool rotational speed of 1005 rpm, tool travel speed of 20 mm/min and the tool tilt angle of 3°. The microstructural analysis, EDX, XRD, and fractograph analysis were done for the confirmation test of FSW joint. Also the corrosion resistance of the weld portion was found with the potentiodynamic polarization test and the same sample was analyzed by image analyzer to reveal the pit formation in the confirmation test weld nugget portion.

Figure 7 presents the macrostructure of the weld nugget portion of confirmation test specimen with the optimized parameter.

Here, the weld zone consists of the middle portion called nugget, the adjacent left is advancing side (AS) which is thermo-mechanically affected zone (TMAZ) and further advancing side is heat affected zone (HAZ). The adjacent right side is called retreating side (RS) which is thermo-mechanically affected zone and further retreating side is heat affected zone. The macroscopic examination confirmed that there was no visible defect in the weldment area. Also, it clearly revealed the different zones of the weld portion and a flat surface on the weldment area. The presence of weld area built-up material (projections) was not to be seen.

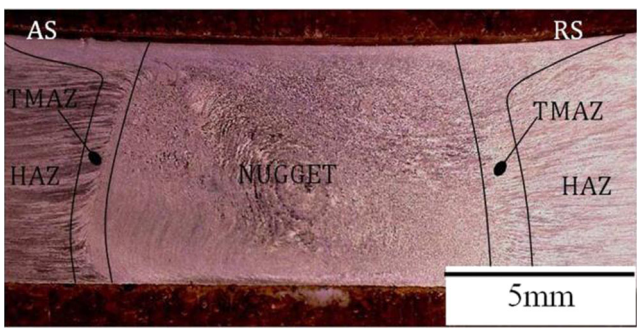

Fig. 7 Macrostructure of hexagonal pin tool—weld confirmation test weld zone

Among the L_9 orthogonal array process parameters and their responses, the 2nd experiment weld joint exhibited better output responses than the other. It exhibited weld strength of 331 MPa (UTS) microhardness of $126Hv_{0.5}$ and Icorr value (corrosion resistance) of 14.4 μA/cm^2. For better understanding, the 2nd experiment weld joint and the confirmation test weld joint were compared in mechanical and microstructural aspect. Figure 8a–c presents the microstructure of advancing side TMAZ, weld nugget and retreating side TMAZ portions of the 2nd experiment weld joint.

Here, the weld nugget portion consisted of coarser grains and the average grain size of 4 μm compared to the confirmation test weld nugget portion. Then, the TMAZ portion consisted of more amounts of undissolute precipitates than the conformation test TMAZ portion. These particles reduced the strength at particular zone. Figure 9a–c presents the microstructure of advancing side TMAZ, weld nugget and retreating side TMAZ portions, respectively.

Figure 9b clearly shows the weld nugget microstructure with ultrafine grain morphology. Also, the grains were equiaxed in shape with the average size 3 μm. The friction stirring action of the hexagonal pin tool generated the pulsating action (100 pulses/s) and ratio of dynamic volume to static volume of the tool pin (volumetric ratio is equal to 1.21). The combination of these forces regenerated coarse grains to ultrafine grain at the joint portion. Owing to ultrafine grain structure and complete dissolved precipitates, the strength of the weld portion got improved in conformation test weld nugget portion than the 2nd experiment weld nugget. Also the volumetric ratio of the tool also led to the proper material flow around the pin at joining portion during FSW. This produces the finer grains in weld nugget and in both side of TMAZ portions. Some coarser dark undissolved precipitates were found in the TMAZ region. But no major changes in the grain structure were found in the HAZ region comparing to the CR AA2219 alloy.

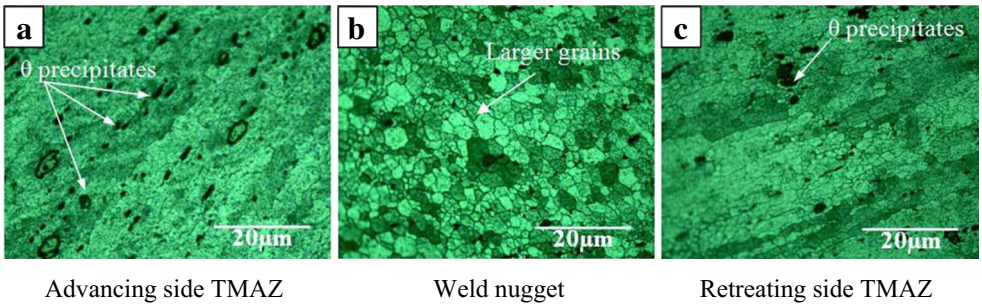

Fig. 8 **a**–**c** Microstructure of 2nd experiment FSW joint

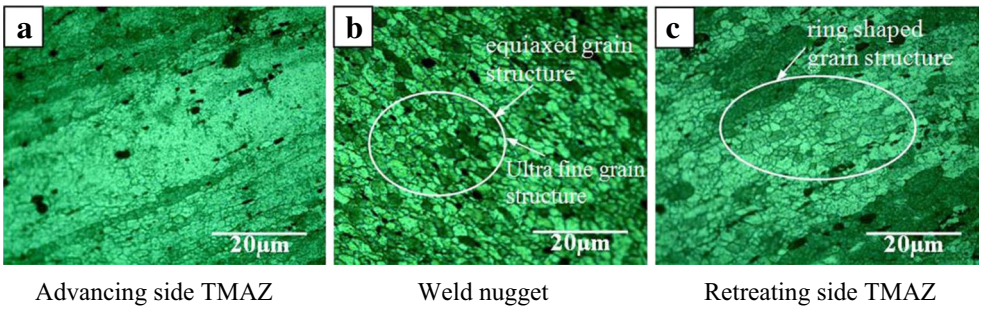

Fig. 9 **a**–**c** Microstructure of confirmation test FSW joint

The TEM analysis was carried out for both weld nuggets of 2nd experiment weld joint and confirmation test weld joint and the same are presented in Fig. 10a, b, respectively. The TEM image of the weld nugget in Fig. 10a, b reveals the metastable intermetallic particles. The complete dissolution of intermetallic particles increased the homogeneity of grains reformation. Generally in an alloy, the coarser intermetallic particles reduce the material's strength and finer or dissolute metastable precipitates increases the strength of the particular zone.

Here, in Fig. 10a, b, weld nugget portion precipitates were varying in size and thickness due to the severe plastic deformation. The coarser θ precipitate particles were fragmented and dissolute within the Al matrix and formed the θ′ and θ″ metastable precipitate particles. Also, the precipitates were categorized by their size and thickness. During the TEM analysis, the selected area diffraction pattern technique was used to classify the θ′ and θ″ particles. The metastable θ″ particles were in the size range of 30 to 120 nm within the thickness range of 8 nm and the θ′ particles were in the size range of 50 to 180 nm with the thickness range of 15 nm and higher size of the precipitates were stable. Here, in Fig. 10b, the confirmation test weld nugget TEM image consists of θ′ and θ″ particles are found and these are Al_2Cu intermetallic particles that improve the strength of the material [23]. Figure 10a majorly consists of θ′ and very few θ″ particles in the weld nugget but a few of stable θ particles are also present.

Figure 11 presents the EDS results of the weld nugget. Here, it is confirmed that the copper element weight percentage of contribution was reduced in the surrounding bulk

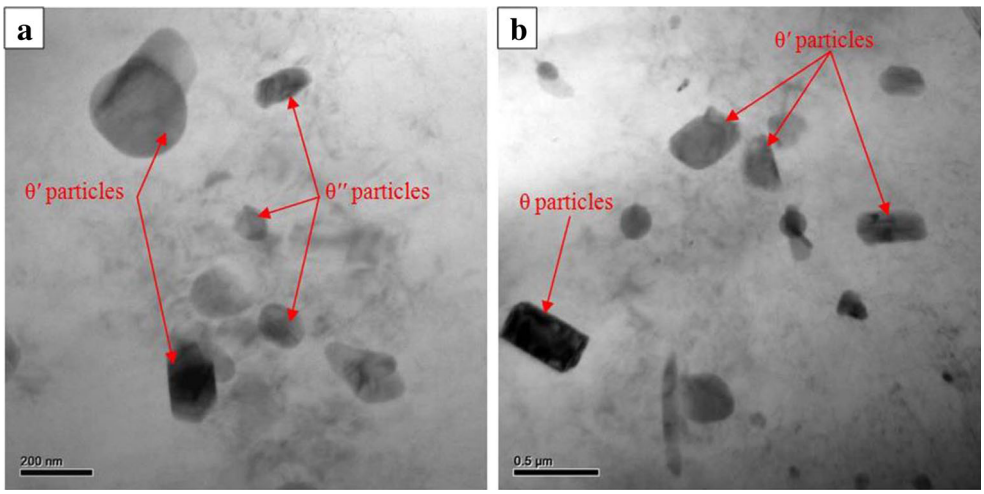

Fig. 10 **a**, **b** TEM image of **a** 2nd experiment WN and **b** conformation test WN

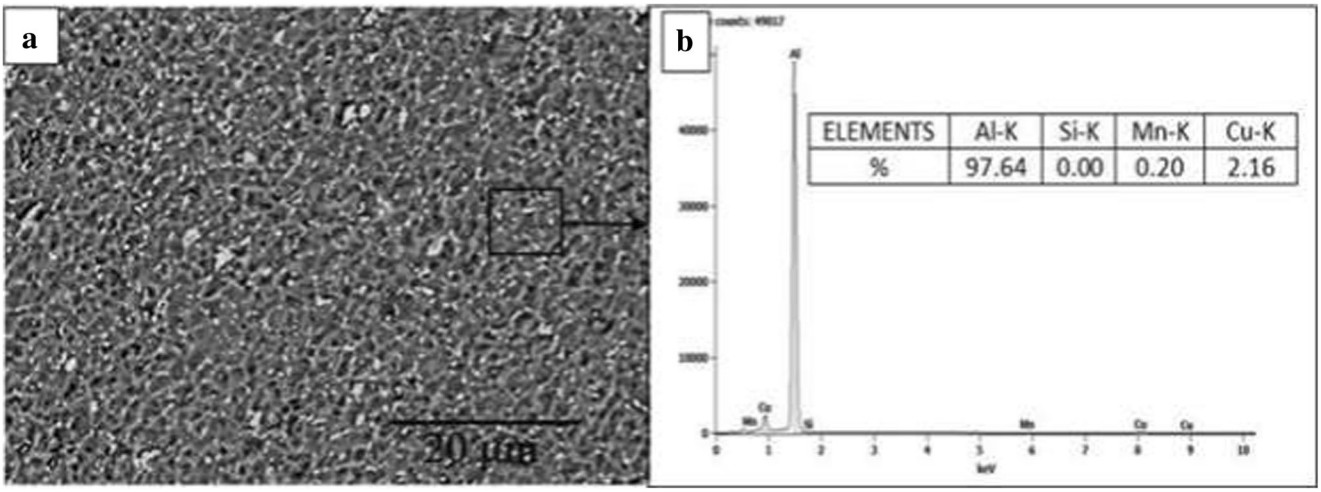

Fig. 11 EDS result of confirmation test weld nugget portion

aluminum matrix. This was the effect of the precipitate dissolution due to the FSW process.

Figure 12 presents the XRD (X-ray diffraction) analysis result. Here, it is revealed that there were no phase changes made in the weld portion material after FSW process. This was due to the low temperature heat input during welding. Also, the XRD plot confirmed that the intensity of the Al_2Cu peaks was reduced due to dissolution of precipitates within the Al matrix.

Tensile test of FSW joint was conducted for the confirmation experiment and it delivered an UTS value of 333.5 MPa, which is better than the 2nd experiment weld joint. Then, the fractured portion of the tensile specimen was analyzed. The SEM fractrographic study of confirmation test specimen is presented in Fig. 13a, b. Here, Fig. 13b was observed with higher magnification. The SEM images show that the fracture surface consisted of the fine dimple structure and dimple coalescence [23]. And no defect was found at the weld fracture surface. It was confirmed that the weld joint failure was of ductile nature. Also the fine dimple structure of the grains is the evidence for the grains size refinement and it leads to the ductile mode of fracture.

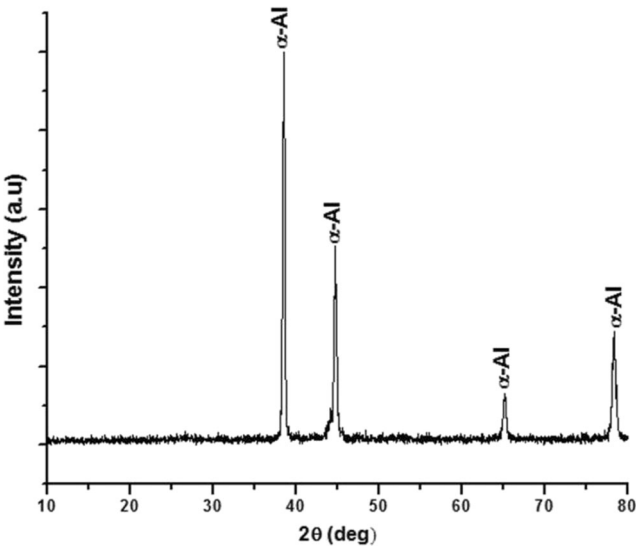

Fig. 12 XRD plot of confirmation test weld nugget

The result of the corrosion analysis of the weld nugget portion is presented in Fig. 14a–c. The potentiodynamic polarization was conducted and the result of the Tafel curve is presented in Fig. 14a. Here, the anodic curve of the tafel first goes in the active region and at certain point, the curve moves on to the continuous passive region. This is because of the strong protective oxide film formation over the corrosion surface. This protects the weld nugget surface against corrosion. The measured corrosion current density was about 13.5 $\mu A/cm^2$. The current density is directly proposal to the corrosion rate and so, weld nugget possess superior corrosion resistance [23]. This was also because of the dissolution of the Al_2Cu precipitates. The SEM image of corroded surface of the weld nugget is presented in Fig. 14b. Here, very tiny pits were found in the weld nugget. This was comparatively much lesser than the other weld joints. Primarily, the corrosion action begins around the intermetallics particles. This is due to the non-cohesive nature of the intermetallics with the surrounding Al matrix. Due to the complete dissolution of precipitate particles during FSW process, it eliminates coarser θ particles in the weld nugget region [23].

Figure 14c presents the results of pit measurement details and surface topography by 3D optical image analyzer. The 3D optical image analyzer was used to find out and analyze the nature of pit formation over the corroded surface of the weld nugget. From the image analysis of the corroded surface topography, it is found that there were very less number of pits and remaining were surface irregularities. From the corroded surface, the notable pit was measured and it had a pit depth of 35.1 µm and width of 32.17 µm. The weld joint made by using optimized process parameters exhibited better mechanical and metallurgical behaviors compared to the L_9 Taguchi experimental weld joints.

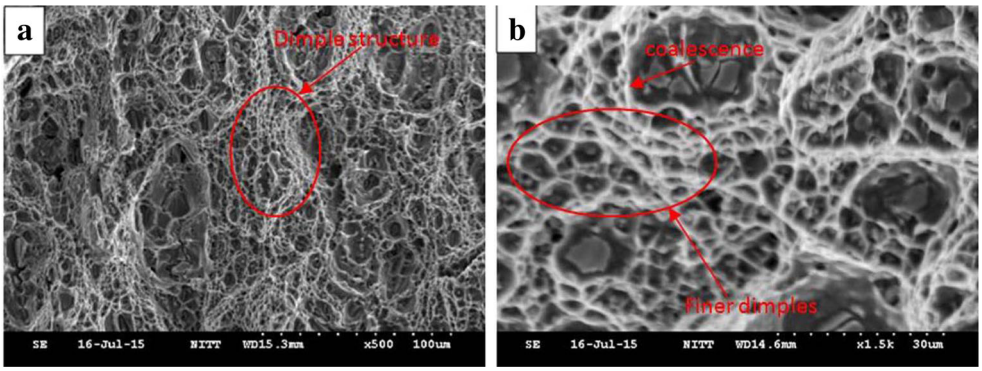

Fig. 13 **a**, **b** Tensile tested fractograph of confirmation test weld joint

4 Conclusions

In the present investigations, the ANN modeling with GA optimization was carried out for ultimate tensile strength, microhardness and corrosion resistance of friction stir welded cryorolled AA2219 alloy. The ANN was used to establish the relationship by supplying the L_9 orthogonal array experimental input and their output responses. Then, the results were further optimized with GA. The following findings were observed from the ANN-GA modeling optimization and the characterization results of FSW joint made with feasible solutions.

- The ANN modeling forecasted the output responses with high accuracy and the least RMSE value was found from the BBP (0.0089991) model with seven numbers of neurons in the hidden layer. If there is more number of training data sets, accuracy of the ANN results will improve. Also the GA was effectively executed to find out the optimized process parameters of FSW.

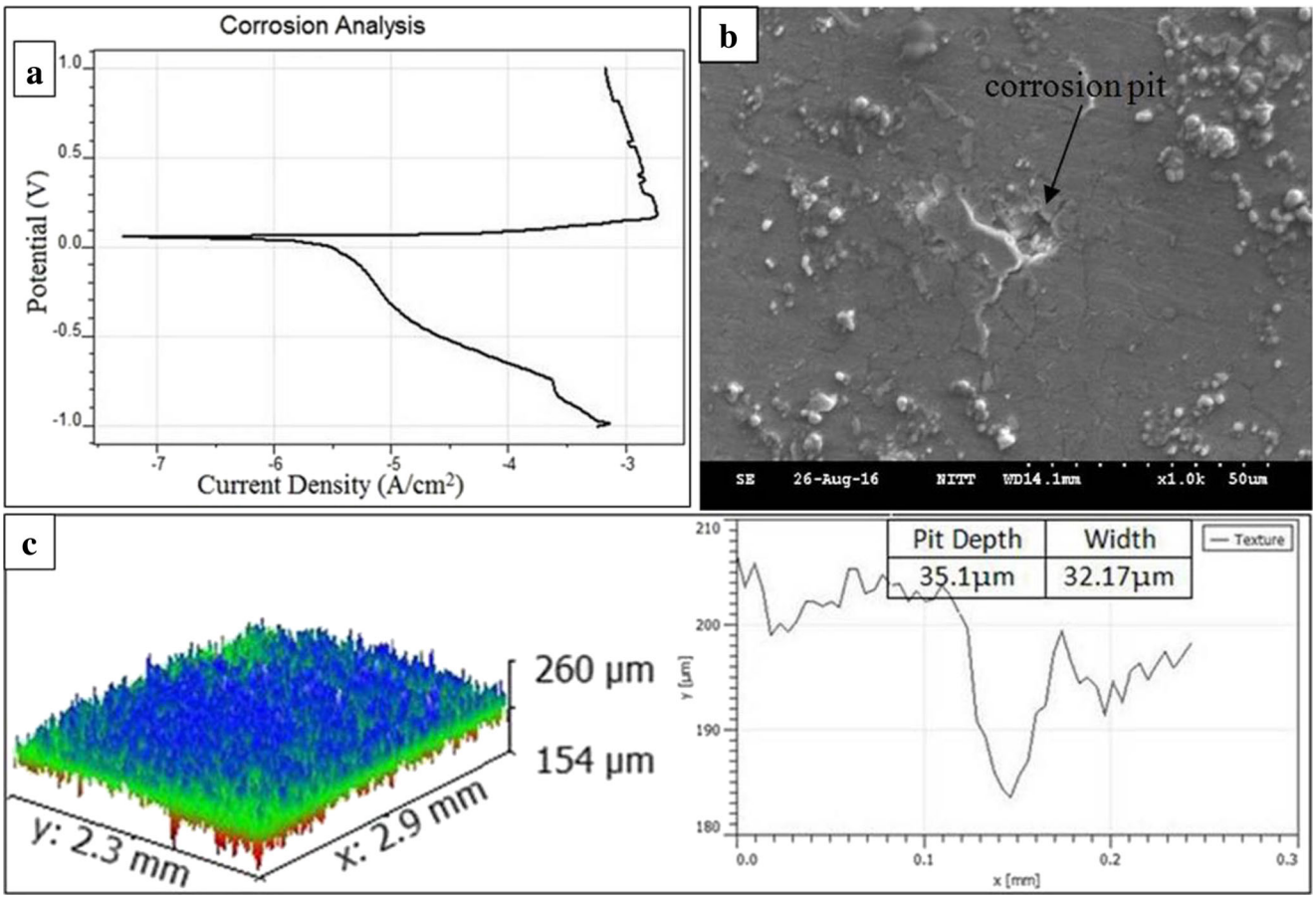

Fig. 14 **a**–**c** Tafel plot curves, SEM image of corroded surface of the confirmation test nugget potion and its depth measurement using image analyzer of FSW nugget, respectively

- The Neural Power professional version 2.5 software provides five ANN modeling algorithms to find the least RMSE value from the least number of inputs with output response and provide the optimal solution. Here, it was possible to feed different combinations of training data sets (80% of the data was selected for training) to train the ANN. The remaining 20% of data can be utilized to check the ability of the model to predict the unknown responses. This methodology provides reliability and verifies the accuracy of the obtained optimal solution.
- The GA gives the feasible input parameters for conformation test and they are rotational speed of 1005 rpm, tool travel speed of 20 mm/min and tool tilt angle of 3°.
- The FSW joint made with feasible solution (confirmation experiment) exhibits tensile strength, microhardness and corrosion current density of 333.5 MPa, 131 $HV_{0.5}$ and 13.5 $\mu A/cm^2$, respectively. The corrosion pit dimensions are also very minimum.

Acknowledgments The authors wish to convey their sincere thanks to the Defence Research & Development Laboratory (DRDL), Ministry of Defence (Government of India), Hyderabad, for the financial support to carry out this research through sponsored project no: DRDL/24/08P/0511/41802. And also, we acknowledge Shri P. Sankaravelayutham, Dy. General Manager, MMD/MME, VSSC, ISRO, Thiruvanandhapuram-695022 for providing the base material for this research work.

References

1. Bozkurt Y (2012) The optimization of friction stir welding process parameters to achieve maximum tensile strength in polyethylene sheets. Mater Des 35:440–445
2. Chien C-H, Lin W-B, Chen T (2011) Optimal FSW process parameters for aluminum alloys AA5083. J Chinese Inst Eng 34:99–105
3. Arora KS, Pandey S, Schaper M, Kumar R (2010) Microstructure evolution during friction stir welding of aluminum alloy AA2219. J Mater Sci Technol 26:747–753
4. Babu S, Elangovan K, Balasubramanian V, Balasubramanian M (2009) Optimizing friction stir welding parameters to maximize tensile strength of AA2219 aluminum alloy joints. Met Mater Int 15:321–330
5. Deepandurai K, Parameshwaran R (2015) Multi response optimization of FSW parameters for cast AA7075/SicP composite. Mater Manuf Process 31:1333–1341
6. Bozkurt Y, Bilici MK (2013) Application of Taguchi approach to optimize of FSSW parameters on joint properties of dissimilar AA2024-T3 and AA5754-H22 aluminum alloys. Mater Des 51: 513–521
7. Shojaeefard MH, Khalkhali A, Akbari M, Tahani M (2013) Application of Taguchi optimization technique in determining aluminum to brass friction stir welding parameters. Mater Des 52:587–592
8. Koilraj M, Sundareswaran V, Vijayan S, Koteswara Rao SR (2012) Friction stir welding of dissimilar aluminum alloys AA2219 to AA5083—optimization of process parameters using Taguchi technique. Mater Des 42:1–7
9. Mohamed MA, Manurung YHP, Berhan MN (2015) Model development for mechanical properties and weld quality class of friction stir welding using multi-objective Taguchi method and response surface methodology. J Mech Sci Technol 29:2323–2331
10. Boulahem K, Salem SB, Bessrour J (2015) Surface roughness model and parametric welding optimization in friction stir welded AA2017 using Taguchi method and response surface methodology. Design and Modeling of Mechanical Systems - II. doi:10.1007/978-3-319-17527-0_9
11. Lakshminarayanan a K, Balasubramanian V (2008) Process parameters optimization for friction stir welding of RDE-40 aluminium alloy using Taguchi technique. Trans Nonferrous Met Soc China 18:548–554
12. Javadi Y, Sadeghi S, Najafabadi MA (2014) Taguchi optimization and ultrasonic measurement of residual stresses in the friction stir welding. Mater Des 55:27–34
13. Shojaeefard MH, Behnagh RA, Akbari M et al (2013) Modelling and pareto optimization of mechanical properties of friction stir welded AA7075/AA5083 butt joints using neural network and particle swarm algorithm. Mater Des 44:190–198
14. Gupta SK, Pandey K, Kumar R (2016) Multi-objective optimization of friction stir welding process parameters for joining of dissimilar AA5083/AA6063 aluminum alloys using hybrid approach. Proc Inst Mech Eng Part L J Mater Des Appl 0:1–11
15. Shojaeefard MH, Akbari M, Asadi P (2014) Multi objective optimization of friction stir welding parameters using FEM and neural network. Int J Precis Eng Manuf 15:2351–2356
16. Dewan MW, Huggett DJ, Warren Liao T et al (2016) Prediction of tensile strength of friction stir weld joints with adaptive neuro-fuzzy inference system (ANFIS) and neural network. Mater Des 92:288–299
17. Yaïci W, Entchev E (2016) Adaptive neuro-fuzzy inference system modelling for performance prediction of solar thermal energy system. Renew Energy 86:302–315
18. Babajanzade Roshan S, Behboodi Jooibari M, Teimouri R et al (2013) Optimization of friction stir welding process of AA7075 aluminum alloy to achieve desirable mechanical properties using ANFIS models and simulated annealing algorithm. Int J Adv Manuf Technol 69:1803–1818
19. Kannan TDB, Ramesh T, Sathiya P (2016) Application of artificial neural network modelling for optimization of Yb: YAG laser welding of Nitinol. Trans Indian Inst Metals. doi:10.1007/s12666-016-0973-x
20. Katherasan D, Jiju V. Elias, Sathiya P, Noorul Haq A (2014) Simulation and parameter optimization of flux cored arc welding using artificial neural network and particle swarm optimization algorithm. J Intell Manuf 25:67–76
21. Abbass MK, Hussein SK, Khudhair AA (2016) Optimization of mechanical properties of friction stir spot welded joints for dissimilar aluminum alloys (AA2024-T3 and AA 5754-H114). Arab J Sci Eng 41:4563–4572
22. Dehabadi VM, Ghorbanpour S, Azimi G (2016) Application of artificial neural network to predict Vickers microhardness of AA6061 friction stir welded sheets. J Cent South Univ 23:2146–2155
23. Babu KK, Panneerselvam K, Sathiya P et al (2016) Experimental investigation on friction stir welding of cryorolled Aa2219 aluminum alloy joints. Surf Rev Lett 24:1750001–1750017
24. Darzi Naghibi H, Shakeri M, Hosseinzadeh M (2016) Neural network and genetic algorithm based modeling and optimization of tensile properties in FSW of AA 5052 to AISI 304 dissimilar joints. Trans Indian Inst Metals 69:891–900
25. Panneerselvam K, Aravindan S, Noorul Haq A (2009) Hybrid of ANN with genetic algorithm for optimization of frictional vibration joining process of plastics. Int J Adv Manuf Technol 42:669–677
26. Tansel IN, Demetgul M, Okuyucu H, Yapici A (2010) Optimizations of friction stir welding of aluminum alloy by using

genetically optimized neural network. Int J Adv Manuf Technol 48: 95–101
27. Anand K, Barik BK, Tamilmannan K, Sathiya P (2015) Artificial neural network modeling studies to predict the friction welding process parameters of Incoloy 800H joints. Eng Sci Technol an Int J 18:394–407
28. Bilgin MB, Meran C, Canyurt OE (2015) Optimization of strength of friction stir welded joints for AISI 430 ferritic stainless steels by genetic algorithm. Int J Adv Manuf Technol 77:2221–2233
29. Kannan TDB, Kannan GR, Kumar BS, Baskar N (2014) Application of artificial neural network modeling for machining parameters optimization in drilling operation. Procedia Mater Sci 5:2242–2249
30. Zhao S, Bi Q, Wang Y, Shi J (2017) Empirical modeling for the effects of welding factors on tensile properties of bobbin tool friction stir-welded 2219-T87 aluminum alloy. Int J Adv Manuf Technol 90:1105–1118
31. Heidarzadeh A, Khodaverdizadeh H, Mahmoudi A, Nazari E (2012) Tensile behavior of friction stir welded AA 6061-T4 aluminum alloy joints. Mater Des 37:166–173
32. Li JQ, Liu HJ (2014) Optimization of welding parameters for the reverse dual-rotation friction stir welding of a high-strength aluminum alloy 2219-T6. Int J Adv Manuf Technol 76:1469–1478
33. Silva ACF, Braga DFO, de Figueiredo MAV, Moreira PMGP (2015) Ultimate tensile strength optimization of different FSW aluminium alloy joints. Int J Adv Manuf Technol 79:805–814
34. Nourani M, Milani AS, Yannacopoulos S (2015) On experimental optimization of friction stir welding of aluminum 6061: understanding processing-microstructure-property relations. Int J Adv Manuf Technol 79:1425–1441
35. Rahimzadeh Ilkhichi A, Soufi R, Hussain G et al (2014) Establishing mathematical models to predict grain size and hardness of the friction stir-welded AA 7020 aluminum alloy joints. Metall Mater Trans B Process Metall Mater Process Sci 46:357–365
36. Heidarzadeh A, Saeid T (2013) Prediction of mechanical properties in friction stir welds of pure copper. Mater Des 52:1077–1087
37. Azizi A, Barenji RV, Barenji AV, Hashemipour M (2016) Microstructure and mechanical properties of friction stir welded thick pure copper plates. Int J Adv Manuf Technol. doi:10.1007/s00170-015-8330-5
38. Karthikeyan R, Balasubramanian V (2010) Predictions of the optimized friction stir spot welding process parameters for joining AA2024 aluminum alloy using RSM. Int J Adv Manuf Technol 51:173–183
39. Heidarzadeh A, Saeid T, Khodaverdizadeh H et al (2013) Establishing a mathematical model to predict the tensile strength of friction stir welded pure copper joints. Metall Mater Trans B Process Metall Mater Process Sci 44:175–183
40. Effertz PS, Quintino L, Infante V (2017) The optimization of process parameters for friction spot welded 7050-T76 aluminium alloy using a Taguchi orthogonal array. Int J Adv Manuf Technol. doi:10.1007/s00170-017-0048-0
41. Heidarzadeh A, Mousavian RT, Khosroshahi RA et al (2017) Empirical model to predict mass gain of cobalt electroless deposition on ceramic particles using response surface methodology. Rare Metals 36:209–219
42. Salari E, Jahazi M, Khodabandeh A, Nanesa HG (2016) Friction stir lap welding of 5456 aluminum alloy with different sheet thickness: process optimization and microstructure evolution. Int J Adv Manuf Technol 82:39–48
43. Yuqing M, Liming K, Fencheng L et al (2017) Effect of tool pin-tip profiles on material flow and mechanical properties of friction stir welding thick AA7075-T6 alloy joints. Int J Adv Manuf Technol 88:949–960
44. Heidarzadeh A, Barenji RV, Esmaily M, Ilkhichi AR (2015) Tensile properties of friction stir welds of AA 7020 aluminum alloy. Trans Indian Inst Metals 68:757–767
45. Babajanzade Roshan S, Behboodi Jooibari M, Teimouri R et al (2013) Optimization of friction stir welding process of AA7075 aluminum alloy to achieve desirable mechanical properties using ANFIS models and simulated annealing algorithm. Int J Adv Manuf Technol 69:1803–1818
46. Heidarzadeh A, Saeid T (2016) Correlation between process parameters, grain size and hardness of friction-stir-welded Cu-Zn alloys. Rare Met 1–11. doi: 10.1007/s12598-016-0704-9
47. Yang T, Xiong J, Chen H (2016) Effect of process parameters on tensile strength in plasma-MIG hybrid welding for 2219 aluminum alloy. Int J Adv Manuf Technol 84:2413–2421
48. Farhanchi M, Neysari M, Vatankhah Barenji R et al (2015) Mechanical activation process for self-propagation high-temperature synthesis of ceramic-based composites: modeling and optimizing using response surface method. J Therm Anal Calorim 122: 123–133
49. Li J, Tao F, Cheng Y, Zhao L (2015) Big data in product lifecycle management. Int J Adv Manuf Technol 81:667–684